

# Detecting electron-phonon couplings during photo-induced phase transition

Takeshi Suzuki<sup>1,\*</sup>, Yasushi Shinohara<sup>2,3</sup>, Yangfan Lu<sup>4</sup>, Mari Watanabe<sup>1</sup>, Jiadi Xu<sup>1</sup>, Kenichi L. Ishikawa<sup>2,3,5</sup>, Hide Takagi<sup>4,6</sup>, Minoru Nohara<sup>7</sup>, Naoyuki Katayama<sup>8</sup>, Hiroshi Sawa<sup>8</sup>, Masami Fujisawa<sup>1</sup>, Teruto Kanai<sup>1</sup>, Jiro Itatani<sup>1</sup>, Takashi Mizokawa<sup>9</sup>, Shik Shin<sup>1,10,11,\*</sup>, and Kozo Okazaki<sup>1,10,\*</sup>

<sup>1</sup>*Institute for Solid State Physics, University of Tokyo, Kashiwa, Chiba 277-8581, Japan*

<sup>2</sup>*Photon Science Center, Graduate School of Engineering, The University of Tokyo, 7-3-1 Hongo, Bunkyo-ku, Tokyo 113-8656, Japan*

<sup>3</sup>*Department of Nuclear Engineering and Management, Graduate School of Engineering, The University of Tokyo, 7-3-1 Hongo, Bunkyo-ku, Tokyo 113-8656, Japan*

<sup>4</sup>*Department of Physics, University of Tokyo, Hongo, Tokyo 113-0033, Japan*

<sup>5</sup>*Research Institute for Photon Science and Laser Technology, The University of Tokyo, 7-3-1 Hongo, Bunkyo-ku, Tokyo 113-0033, Japan*

<sup>6</sup>*Max Planck Institute for Solid State Research, Heisenbergstrasse 1, 70569 Stuttgart, Germany*

<sup>7</sup>*Research Institute for Interdisciplinary Science, Okayama University, Okayama, 700-8530, Japan*

<sup>8</sup>*Department of Applied Physics, Nagoya University, Nagoya 464-8603, Japan*

<sup>9</sup>*School of Advanced Science and Engineering, Waseda University, Shinjuku, Tokyo  
169-8555, Japan*

<sup>10</sup>*AIST-UTokyo Advanced Operando-Measurement Technology Open Innovation  
Laboratory (OPERAND-OIL), Kashiwa, Chiba 277-8581, Japan*

<sup>11</sup>*Office of University Professor, The University of Tokyo, Kashiwa, Chiba 277-8581,  
Japan*

\*To whom correspondence should be addressed. E-mail: [takeshi.suzuki@issp.u-tokyo.ac.jp](mailto:takeshi.suzuki@issp.u-tokyo.ac.jp); [shin@issp.u-tokyo.ac.jp](mailto:shin@issp.u-tokyo.ac.jp); [okazaki@issp.u-tokyo.ac.jp](mailto:okazaki@issp.u-tokyo.ac.jp).

**Photo-induced phase transitions have been intensively studied owing to the ability to control a material of interest in a flexible manner, which can induce exotic phases unable to be attained at equilibrium [1] [2] [3] [4] [5]. The key mechanisms are still under debate, and how the couplings between the electron, lattice, and spin degrees of freedom are evolving during photo-induced phase transitions has currently been a central issue [6]. However, the measurements for each degree in the ultrafast timescale require distinctively different and state-of-the-art techniques, such as terahertz spectroscopy for low frequency conductivity [3] [7], time- and angle-resolved photoemission spectroscopy for electronic band structures [8] [9], and time-resolved X-ray measurements for crystal structures [10] [11] [12], which prevents directly revealing the connections between each degree in the nonequilibrium state. Here, we develop a new analysis method, frequency-domain angle-resolved photoemission spectroscopy, to gain precise insight into electron-phonon couplings in photo-induced insulator-to-metal transitions. Regarding the electron-phonon coupling in the photo-induced insulator-to-metal transition for Ta<sub>2</sub>NiSe<sub>5</sub>, we find**

**that multiple coherent phonons are generated as a result of displacive excitations, and they show band-selective coupling to the electrons. The lattice modulation corresponding to the specific phonon mode, where Ta lattice is sheared along the a-axis, is the most relevant for the formation of excitonic insulator phase and is the most effective to modulate the valence band top in the photo-induced semimetallic phase. Furthermore, we developed a new theoretical method to analyse the mode and momentum selective electron-phonon couplings based on the density functional theory. Our novel analysis method can pave the way for quantum engineering utilizing correlations between electrons and phonons.**

Strongly-correlated electron systems display very rich phases owing to intertwined couplings between multiple degrees of freedom including the charge, orbital, spin, and lattice [13]. Moreover, external fields, such as electronic and magnetic fields or physical pressure, can induce phase transitions in these systems by breaking their subtle balances between multiple competing phases [14] [15]. In this respect, photo-excitation is a very promising way to control the physical properties because it can instantaneously change physical properties of a targeting material in various manners by exploiting many degrees of freedom such as polarization or wavelength. For studying photo-excited nonequilibrium states, time- and angle-resolved photoemission spectroscopy (ARPES) has a strong advantage because it can track nonequilibrium electronic band structures after photoexcitations [8] [9] [16] [17].

For photo-induced phase transitions, although many strongly-correlated electron systems have been intensively studied, the precise mechanisms are still under debate [18] [19] [20]. Recently, we revealed the photo-induced insulator-to-metal transitions (IMTs)

in Ta<sub>2</sub>NiSe<sub>5</sub> [21], where we also showed strong evidence in dynamical behaviours as an excitonic insulator. Moreover, other interesting photo-excited phenomena in Ta<sub>2</sub>NiSe<sub>5</sub> have been reported previously, which include photo-induced enhancement of the excitonic insulator [22] [23] or emergence of collective modes [24] [25]. In most reports, the key roles for such phenomena are played by significant electron-phonon couplings.

Here we report a novel analysis method, namely, frequency-domain angle-resolved photoemission spectroscopy (FDARPES), to reveal how electron-phonon couplings play roles in the photo-excited nonequilibrium states for Ta<sub>2</sub>NiSe<sub>5</sub>. We observe that the lattice modulation corresponding to the phonon mode, where Ta lattice is sheared along the *a*-axis, is the most relevant for the photo-induced semimetallic state. Our analysis method also provides a new playground for the theoretical calculations of electron-phonon couplings.

TARPES, as illustrated in Fig. 1a, allows us to directly observe the temporal evolution of the electronic band structure. Figure 1b–1e show the TARPES snapshots of Ta<sub>2</sub>NiSe<sub>5</sub> at various delays shown as a function of momentum and energy. The delay between the pump and probe is indicated in each panel. To enhance the temporal variations, the difference images between the before and after photoexcitation are shown in Fig. 1f–1h, where red and blue represent an increase and decrease in photoemission intensity, respectively. After strong photoexcitation of 2.27 mJ cm<sup>-2</sup>, new semimetallic electron- and hole-dispersions appear, as has previously been reported [21]. This is the direct signature of photo-induced IMT. To highlight the change of the electronic band structure, we show the peak positions of the TARPES spectra before and after photoexcitation in Figs. 2a and 2b. One can notice that the hole band is shifted upward and crosses the Fermi

level,  $E_F$ , while the electron band appears and crosses  $E_F$  at the same Fermi wavevector,  $k_F$ , as the hole band.

To more specifically reveal the photo-induced profile in  $\text{Ta}_2\text{NiSe}_5$ , we investigated the TARPES images in terms of electron-phonon couplings. Figure 2c shows the time-dependent intensities for representative regions in the energy and momentum space indicated as I–IV in Fig. 2a and 2b. As a background, carrier dynamics corresponding to overall rise-and-decay or decay-and-rise behaviours were observed. Additionally, oscillatory behaviours were clearly seen superimposed onto background carrier dynamics, which indicated strong electron-phonon couplings as a result of excitations of coherent phonons. To extract the oscillatory components, we first fit the carrier dynamics to a double-exponential function convoluted with a Gaussian function, shown as the black-solid lines in Fig. 2c, and then subtracted the fitting curves from the data. Fourier transformations were performed for the subtracted data and the intensities for each frequency component are shown in Fig. 2d. One can clearly see that distinctively different frequency-dependent peak structures appeared depending on the regions in the energy and momentum space denoted as I–IV in Fig. 2a and 2b.

Considering that the frequencies for the peak positions observed in this work matched the  $A_g$  phonon modes reported in previous work [26] [27] and that we dominantly excited the electron system under our experimental condition, the observed coherent phonons were likely to arise from displacive excitation of coherent phonons (DECPs) [28]. According to the DECP theory, photoexcitation suddenly changes the minimum energy position in the lattice coordinates of the potential energy surface (PES), and lattice coordinates oscillate around the new energy minimum position with its own frequency

determined by the curvature of the PES. Figure 2e schematically shows this situation. The ground and excited states are denoted as  $|G\rangle$  and  $|E\rangle$ , respectively, while  $Q_{2\text{ THz}}$  and  $Q_{3\text{ THz}}$  are the lattice coordinates corresponding to the 2-THz and 3-THz phonon modes.

To investigate the phases of coherent phonons, we further fitted the oscillatory components by single-cosine function. Figure 2f and 2g shows the results for regions I and II, in which the 3- and 2-THz components exhibited the strongest peaks, respectively. Phases and frequencies were obtained as  $-0.19 \pm 0.11 \pi$  and  $2.97 \pm 0.02$  THz for region I, and  $0.37 \pm 0.12 \pi$  and  $2.07 \pm 0.02$  THz for region II, respectively. If the change of PES accompanies no delay from the laser excitation, DECP has a cosine-like behaviour, that is, the expected phase is  $0 \pi$ . Thus, the modulation of photoemission intensity in region I along the 3-THz phonon mode was triggered immediately after photoexcitation. However, the relatively positive phase shift in region II compared with region I indicated the modulation of the photoemission intensity along the 2-THz phonon mode occurred with a delay of 120 fs.

We will now discuss the electron-phonon couplings in more detail. Since we observed that the amplitude of each oscillation significantly changed depending on the regions in the energy and momentum space, we further mapped out the frequency-dependent intensity of the Fourier component in the energy and momentum space, which we call FDARPES. Figure 3a–3e shows the FDARPES spectra corresponding to the frequencies of 1, 2, 3, 3.75, and 4 THz, respectively. The corresponding phonon modes were calculated by *ab initio* calculation and their modes are shown in Fig. 3f–3j. We assigned all the phonon modes as  $A_g$  modes, while 2- and 3.75-THz modes have previously been

assigned as  $B_g$  modes [25]. Our detailed assignment procedure is provided in Supplementary Information.

Noticeably, the FDARPES spectra exhibited distinctively different behaviour depending on the frequency, which demonstrated that each phonon mode was selectively coupled to the specific electronic bands. Furthermore, the 2-THz phonon mode had the strongest signal around  $E_F$ , which consisted of a mixture of Ta  $5d$  and Se  $3p$  orbitals [29], and was responsible for the collapse of the excitonic insulator. Because the IMT of  $\text{Ta}_2\text{NiSe}_5$  occurs by melting the excitonic insulating flat band, this strongest signal suggested that the photo-induced metallic states drive the lattice distortions corresponding to the 2-THz phonon motion.

To gain more quantitative insight into electron-phonon couplings engraved in the FDARPES spectra, we performed density functional theory (DFT) calculations to obtain  $dE/dQ$ , which represents how much the energy of the band structure shifts ( $dE$ ) with respect to the lattice modulation corresponding to the direction of each phonon mode ( $dQ$ ). Figure 4a–4e show the FDARPES spectra and  $dE/dQ$ . It should be noted that the FDARPES spectra were well correlated with  $dE/dQ$ . From the comparison, we noticed that the 2-THz phonon mode, which corresponded to Ta movements in the  $a$ -axis direction, dominantly affected the flat band, while the 3-THz phonon mode, which corresponded to Se movements in the  $a$ -axis, exhibited significant effects on the side bands lying around  $(E-E_F, k) = (-0.6 \text{ eV}, \pm 0.4 \text{ \AA}^{-1})$ .

As clearly seen in this work, our developed analysis method, FDARPES, can offer new opportunities to investigate the electron-phonon couplings through the non-equilibrium

states. Our work using this method provides direct evidence for the DECP mechanisms responsible for the photo-induced IMTs in  $\text{Ta}_2\text{NiSe}_5$ . Thus, FDARPES can be used to study many other photo-induced phase transitions by observing how the electron band structure is influenced by the specific phonon-mode. We also emphasize the versatility of FDARPES. By using the multiple degrees of freedom in the excitation pulses, we can drive different quasiparticles; for example, circularly-polarized pulses can promote specific a spin population or appropriate mid- and far-infrared wavelength can resonantly excite IR-active phonons. Furthermore, FDARPES can detect couplings of electrons to any quasiparticles or collective modes as long as their couplings manifest as oscillations of intensities in the TARPES spectra.

## Methods

**Sample preparation.** High-quality single crystals of  $\text{Ta}_2\text{Ni}(\text{Se}_{0.097}\text{S}_{0.03})_5$  and  $\text{Ta}_2\text{NiSe}_5$  were grown by chemical vapour transport method using  $\text{I}_2$  as transport agent, as was reported in the refs. [30] [31]. Whereas a relatively large cleaved surface is necessary for TARPES measurements compared with static ARPES, because  $\text{Ta}_2\text{NiSe}_5$  has a one-dimensional crystal structure, a large cleaved surface of the pristine  $\text{Ta}_2\text{NiSe}_5$  that was sufficient for TARPES measurements was difficult to obtain. However, sufficiently-large cleaved surfaces of 3% S-substituted  $\text{Ta}_2\text{NiSe}_5$  and  $\text{Ta}_2\text{NiS}_5$  could be obtained. This is why we used 3% S-substituted  $\text{Ta}_2\text{NiSe}_5$  rather than pristine  $\text{Ta}_2\text{NiSe}_5$  in this study. Clean surfaces were obtained by cleaving *in situ*.

**Photoemission measurements.** To characterise the sample, static angle-resolved photoemission spectroscopy measurements were performed by using a He discharge lamp and a hemispherical electron analyser (Omicron-Scienta R4000) with an energy resolution of  $\sim 12.5$  meV. For the TARPES measurements, we used an extremely stable commercial Ti:sapphire regenerative amplifier system (Spectra-Physics, Solstice Ace) with a centre wavelength of 800 nm and pulse width of  $\sim 35$  fs for the pump pulse. Second harmonic pulses generated in a 0.2-mm-thick crystal of  $\beta$ -BaB<sub>2</sub>O<sub>4</sub> were focused into a static gas cell filled with Ar to generate higher harmonics. By using a set of SiC/Mg multilayer mirrors, we selected the seventh harmonic of the second harmonic ( $h\nu = 21.7$  eV) for the probe pulse. The temporal resolution was determined to be  $\sim 70$  fs from the TARPES intensity far above the Fermi level, which corresponded to the cross correlation between the pump and probe pulses. All the measurements in this work were performed at the temperature of 100 K.

**DFT calculation for phonon mode.** Theoretical calculations for the band structure and a structure optimization relied on density functional theory [32] with the Perdew-Burke-Ernzerhof functional [33]. The simulations were performed by the abinit code [34] based on a norm-conserving pseudopotential with the Troullier–Martin type separable form provided by the fhi98PP program [35]. Initially, atomic positions were optimized in the same primitive cell shape as an experimental structure. Density-Functional-Perturbation-Theory (DFPT) [36] calculation was performed to obtain the normal modes of the phonon. Band calculations were performed for the optimized position and the positions where the atomic positions were distorted along the normal mode, one direction and then the opposite direction. Energy cut-off and number of Brillouin zone sampling were taken as 1361 eV and  $24 \times 24 \times 12$  for the primitive cell expected for the DFPT calculation.

**Data availability.** The data supporting the findings of this study are available from the corresponding author.

**Acknowledgements** We would like to acknowledge Y. Ohta, for valuable discussions and comments. This work was supported by Grants-in-Aid for Scientific Research (KAKENHI) (Grant No. 18K13498, 19H00659, 19H01818, 19H00651 18K14145, and 19H02623) from the Japan Society for the Promotion of Science (JSPS), by JSPS KAKENHI on Innovative Areas “Quantum Liquid Crystals” (Grant No. 19H05826), by the Center of Innovation Program from the Japan Science and Technology Agency, JST, the Research and Education Consortium for Innovation of Advanced Integrated Science by JST, and by MEXT Quantum Leap Flagship Program (MEXT Q-LEAP) (Grant No. JPMXS0118067246, JPMXS0118068681), Japan. The computation in this work has been done using the facilities of the Supercomputer Center, The Institute for Solid State Physics, The University of Tokyo.

**Author Contributions** T.S., M.W., and J.X. conducted the TARPES measurements. T.S. analysed the data. Y.S. performed the DFT calculations. M.F., T.K., and J.I. maintained the HHG laser system and improved the TARPES apparatus. Y.F.L., H.T., M.N., N.K., and H.S. grew high-quality single crystals and characterized them. T.S., Y.S., K.L.I, S.S., and K.O. wrote the manuscript. K.L.I., S.S., and K.O. designed the project. All authors discussed the results and contributed to the manuscript.

1. Miyano, K., Tanaka, T., Tomioka, Y. & Tokura, Y. Photoinduced Insulator-to-Metal Transition in a Perovskite Manganite. *Phys. Rev. Lett.* **78**, 4257 (1997).
2. Collet, E., Lemée-Cailleau, M.-H., and Buron-Le Cointe, M., Cailleau, H., Wulff, M., Luty, T., Koshihara, S., Meyer, M., Toupet, L., Rabiller, P., & Techert, S. Laser-Induced Ferroelectric Structural Order in an Organic Charge-Transfer Crystal. *Science*, **300**, 612 (2003).
3. Fausti, D., Tobey, R. I., Dean, N., Kaiser, S., Dienst, A., Hoffmann, M. C., Pyon, S., Takayama, T., Takagi, H. & Cavalleri, A. Light-Induced Superconductivity in a Stripe-Ordered Cuprate. *Science* **331**, 189 (2011).
4. Frigge, T., Hafke, B., Witte, T., Krenzer, B., Streubühr, C., Samad Syed, A., Mikšić Trontl, V., Avigo, I., Zhou, P., Ligges, M., Linde, D., Bovensiepen, U., Horn-von Hoegen, M., Wippermann, S., Lücke, A., Sanna, S., Gerstmann, U., & Schmidt, W. G. Optically excited structural transition in atomic wires on surfaces at the quantum limit. *Nature*, **544**, 207 (2017).
5. Zong, A., Kogar, A., Bie, Y.-Q., Rohwer, T., Lee, C., Baldini, E., Ergeçen, E., Yilmaz, M. B., Freelon, B., Sie, E. J., Zhou, H., Straquadine, J., Walmsley, P., Dolgirev, P. E., Rozhkov, A. V., Fisher, I. R., Jarillo-Herrero, P., Fine, B. V., & Gedik, N. Evidence for topological defects in a photoinduced phase transition. *Nat. Phys.*, **15** 27 (2019).
6. Basov, D. N., Averitt, R. D. & Hsieh, D. Towards properties on demand in quantum materials. *Nat. Mat.* **16**, 1017 (2017).
7. Mitrano, M., Cantaluppi, A., Nicoletti, D., Kaiser, S., Perucchi, A., Lupi, S., Di Pietro, P., Pontiroli, D., Riccò, M., Clark, S. R., Jaksch, D. & Cavalleri, A. Possible light-induced superconductivity in K<sub>3</sub>C<sub>60</sub> at high temperature. *Nature* **530**, 461 (2016).

8. Rohwer, T., Hellmann, S., Wiesenmayer, M., Sohrt, C., Stange, A., Slomski, B., Carr, A., Liu, Y., Avila, L. M., Kallane, M., Mathias, S., Kipp, L., Rossnagel, K. & Bauer M. Collapse of long-range charge order tracked by time-resolved photoemission at high momenta. *Nature*, **471**, 490 (2011).
9. Hellmann, S., Rohwer, T., Kalläne, M., Hanff, K., Sohrt, C., Stange, A., Carr, A., Murnane, M. M., Kapteyn, H. C., Kipp, L., Bauer, M. & Rossnagel, K. Time-domain classification of charge-density-wave insulators. *Nat. Commun.* **3**, 1069 (2012).
10. Mankowsky, R., Subedi, A., Forst, M., Mariager, S. O., Chollet, M., Lemke, H. T., Robinson, J. S., Glownia, J. M., Minitti, M. P., Frano, A., Fechner, M., Spaldin, N. A., Loew, T., Keimer, B., Georges, A. & Cavalleri, A. Nonlinear lattice dynamics as a basis for enhanced superconductivity in  $\text{YBa}_2\text{Cu}_3\text{O}_{6.5}$ . *Nature* **516**, 71 (2014).
11. Gerber, S., Kim, K. W., Zhang, Y., Zhu, D., Plonka, N., Yi, M., Dakovski, G. L., Leuenberger, D., Kirchmann, P. S., Moore, R. G., Chollet, M., Glownia, J. M., Feng, Y., Lee, J.-S., Mehta, A., Kemper, A. F., Wolf, T., Chuang, Y.-D., Hussain, Z., Kao, C.-C., Moritz, B., Shen, Z.-X., Devereaux, T. P. & Lee, W.-S. Direct characterization of photoinduced lattice dynamics in  $\text{BaFe}_2\text{As}_2$ . *Nat. Commun.* **6**, 7377 (2015).
12. Gerber, S., Yang, S.-L., Zhu, D., Soifer, H., Sobota, J. A., Rebec, S., Lee, J. J., Jia, T., Moritz, B., Jia, C., Gauthier, A., Li, Y., Leuenberger, D., Zhang, Y., Chaix, L., Li, W., Jang, H., Lee, J.-S., Yi, M., Dakovski, G. L., Song, S., Glownia, J. M., Nelson, S., Kim, K. W., Chuang, Y.-D., Hussain, Z., Moore, R. G., Devereaux, T. P., Lee, W.-S., Kirchmann, P. S. & Shen, Z.-X. Femtosecond electron-phonon lock-in by photoemission and x-ray free-electron laser. *Science* **357**, 71 (2017).

13. Tokura, Y., Kawasaki, M. & Nagaosa, N. Emergent functions of quantum materials, *Nat. Phys.* **13**, 1056 (2017).
14. Sow, C., Yonezawa, S., Kitamura, S., Oka, T., Kuroki, K., Nakamura, F., and Maeno, Y. Current-induced strong diamagnetism in the Mott insulator  $\text{Ca}_2\text{RuO}_4$ , *Science* **358**, 1084 (2017).
15. Matsuura, K., Mizukami, Y., Arai, Y., Sugimura, Y., Maejima, N., Machida, A., Watanuki, T., Fukuda, T., Yajima, T., Hiroi, Z., Yip, K. Y., Chan, Y. C., Niu, Q., Hosoi, S., Ishida, K., Mukasa, K., Kasahara, S., Cheng, J.-G., Goh, S. K., Matsuda, Y., Uwatoko, Y., & Shibauchi, T. *Nat. Commun.* **8**, 1143 (2017).
16. Schmitt, F., Kirchmann, P. S., Bovensiepen, U., Moore, R. G., Rettig, L., Krenz, M., Chu, J.-H., Ru, N., Perfetti, L., Lu, D. H., Wolf, M., Fisher, I. R., & Shen, Z.-X., *Science* **321**, 1649 (2008).
17. Suzuki, T., Iimori, T., Ahn, S. J., Zhao, Y., Watanabe, M., Xu, J., Fujisawa, M., Kanai, T., Ishii, N., Itatani, J., Suwa, K., Fukidome, H., Tanaka, S., Ahn, J. R., Okazaki, K., Shin, S., Komori, F. & Matsuda, I. *ACS Nano* **13**, 11981 (2019).
18. Gedik, N., Yang, D.-S., Logvenov, G. Bozovic, and I., Zewail, A. H., Nonequilibrium Phase Transitions in Cuprates Observed by Ultrafast Electron Crystallography, *Science* **316**, 425 (2007).
19. Morrison, V. R., Chatelain, R. P., Tiwari, K. L., Hendaoui, A., Bruhács, A., Chaker, M., and Siwick, B. J., A photoinduced metal-like phase of monoclinic  $\text{VO}_2$  revealed by ultrafast electron diffraction, *Science* **346**, 445 (2014).

20. Ichikawa, H., Nozawa, S., Sato, T., Tomita, A., Ichiyanagi, K., Chollet, M., Guerin, L., Dean, N., Cavalleri, A., Adachi, S., Arima, T., Sawa, H., Ogimoto, Y., Nakamura, M., Tamaki, R., Miyano, K., and Koshihara, S., Transient photoinduced 'hidden' phase in a manganite, *Nat. Mat.* **10**, 101 (2011).
21. Okazaki, K., Ogawa, Y., Suzuki, T., Yamamoto, T., Someya, T., Michimae, S., Watanabe, M., Lu, Y., Nohara, M., Takagi, H., Katayama, N., Sawa, H., Fujisawa, M., Kanai, T., Ishii, N., Itatani, J., Mizokawa, T. & Shin, S. Photo-induced semimetallic states realised in electron-hole coupled insulators. *Nat. Commun.* **9**, 4322 (2018).
22. Mor, S., Herzog, M., Golež, D., and Werner, P., Eckstein, M., Katayama, N., Nohara, M., Takagi, H., Mizokawa, T., Monney, C. Stähler, J. Ultrafast Electronic Band Gap Control in an Excitonic Insulator. *Phys. Rev. Lett.* **8**, 086401 (2017).
23. Tanabe, T., Sugimoto, K., Ohta, Y. Nonequilibrium dynamics in the pump-probe spectroscopy of excitonic insulators. *Phys. Rev. B* **98**, 235127 (2018).
24. Murakami, Y., Golež, D., Eckstein, M. & Werner, P. Photoinduced enhancement of excitonic order. *Phys. Rev. Lett.* **8**, 086401 (2017).
25. Werdehausen, D., Takayama, T., Höppner, M., Albrecht, G., Rost, A. W., Lu, Y. Manske, D., Takagi, H. & Kaiser, S. *Sci. Adv.* **4**, eaap8652 (2018).
26. Kim, S., Y., Kim, Y., Kang, C. -J., An, E., -S., Kim, H., K., Eom, M. J., Lee, M., Park, C., Kim, T., -H., Choi, H., C., Min, B., I. & Kim, J. S. Layer-Confined Excitonic Insulating Phase in Ultrathin Ta<sub>2</sub>NiSe<sub>5</sub> Crystals. *ACS Nano* **10**, 8888 (2016).

27. Mor, S., Herzog, M., Noack, J., Katayama, N., Nohara, M., Takagi, H., Trunschke, A., Mizokawa, T., Monney, C. & Stähler, J. Inhibition of the photoinduced structural phase transition in the excitonic insulator Ta<sub>2</sub>NiSe<sub>5</sub>. *Phys. Rev. B* **97**, 115154 (2018).
28. Zeiger, H. J., Vidal, J., Cheng, T. K., Ippen, E. P., Dresselhaus, G. & Dresselhaus, M. S. Theory for displacive excitation of coherent phonons. *Phys. Rev. B* **45**, 768 (1992).
29. Lee, J., Kang, C. -J. and Eom, M. J., Kim, J. S., Min, B. I. & Yeom, H. W. Strong interband interaction in the excitonic insulator phase of Ta<sub>2</sub>NiSe<sub>5</sub>. *Phys. Rev. B* **99**, 075408 (2019).
30. Lu, Y. F., Kono, H., Larkin, T. I., Rost, A. W., Takayama, T., Boris, A. V., Keimer, B., and Takagi, H. Zero-gap semiconductor to excitonic insulator transition in Ta<sub>2</sub>NiSe<sub>5</sub>. *Nat. Commun.* **8**, 14408 (2017).
31. Nakano, A., Sugawara, K., Tamura, S., Katayama, N., Matsubayashi, K., Okada, T., Uwatoko, Y., Munakata, K., Nakao, A., Sagayama, H., Kumai, R., Sugimoto, K., Maejima, N., Machida, A., Watanuki, T. & Sawa, H. *IUCrJ* **5**, 158 (2018).
32. Hohenberg P. & Kohn, W. Inhomogeneous Electron Gas, *Phys. Rev.* **136**, B864 (1964).
33. Perdew, J. P., Burke, K., & Ernzerhof, M. Generalized Gradient Approximation Made Simple. *Phys. Rev. Lett.* **77**, 3865 (1996).
34. Gonze, X., *et al.*, Recent developments in the ABINIT software package. *Comput. Phys. Commun.* **205**, 106 (2016).

35. Fuchs, M. & Scheffler, M. Ab initio pseudopotentials for electronic structure calculations of poly-atomic systems using density-functional theory. *Comput. Phys. Commun.* **119**, 67 (1999).
36. Baroni, S., de Gironcoli, S., Dal Corso, A., & Giannozzi, P. Phonons and related crystal properties from density-functional perturbation theory. *Rev. Mod. Phys.* **73**, 515 (2001).

**Supplementary Information** accompanies the paper on [www.nature.com/nature](http://www.nature.com/nature).

**Additional Information** Correspondence and requests for materials should be addressed to T.S. ([takeshi.suzuki@issp.u-tokyo.ac.jp](mailto:takeshi.suzuki@issp.u-tokyo.ac.jp)), S.S. ([shin@issp.u-tokyo.ac.jp](mailto:shin@issp.u-tokyo.ac.jp)), K.O. ([okazaki@issp.u-tokyo.ac.jp](mailto:okazaki@issp.u-tokyo.ac.jp)).

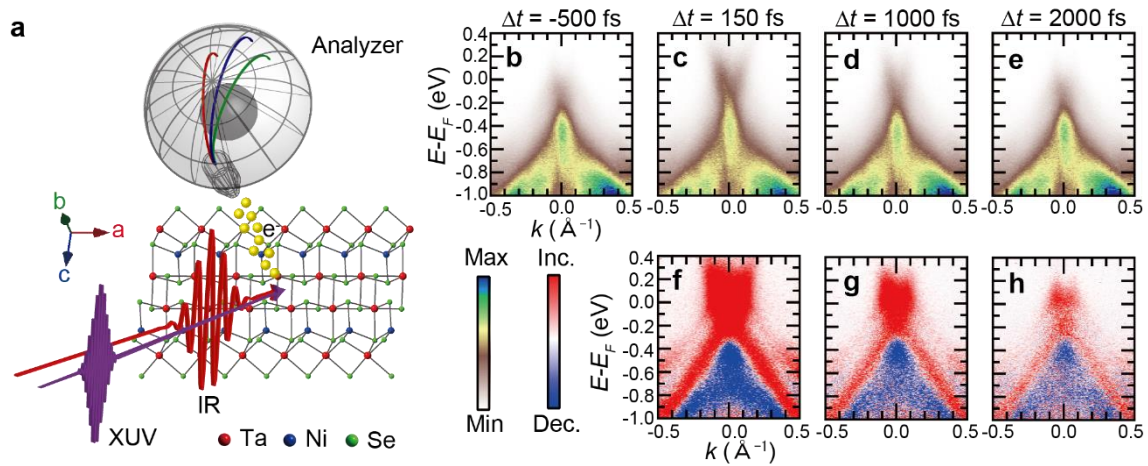


**Figure 1 | Experimental setup and TARPES spectra of  $\text{Ta}_2\text{NiSe}_5$ .** **a**, Schematic illustration of time- and angle-resolved photoemission spectroscopy (TARPES), as applied to  $\text{Ta}_2\text{NiSe}_5$ . The pump pulse is infrared light whereas the probe pulse is extreme ultraviolet light produced by high-harmonic generation. Photoelectrons are detected by a hemisphere analyser. **b-e**, TARPES spectra of  $\text{Ta}_2\text{NiSe}_5$ . The delay time between the pump and probe is indicated in each panel. **f-h**, Difference images of TARPES. Red and blue points represent increasing and decreasing photoemission intensity, respectively.

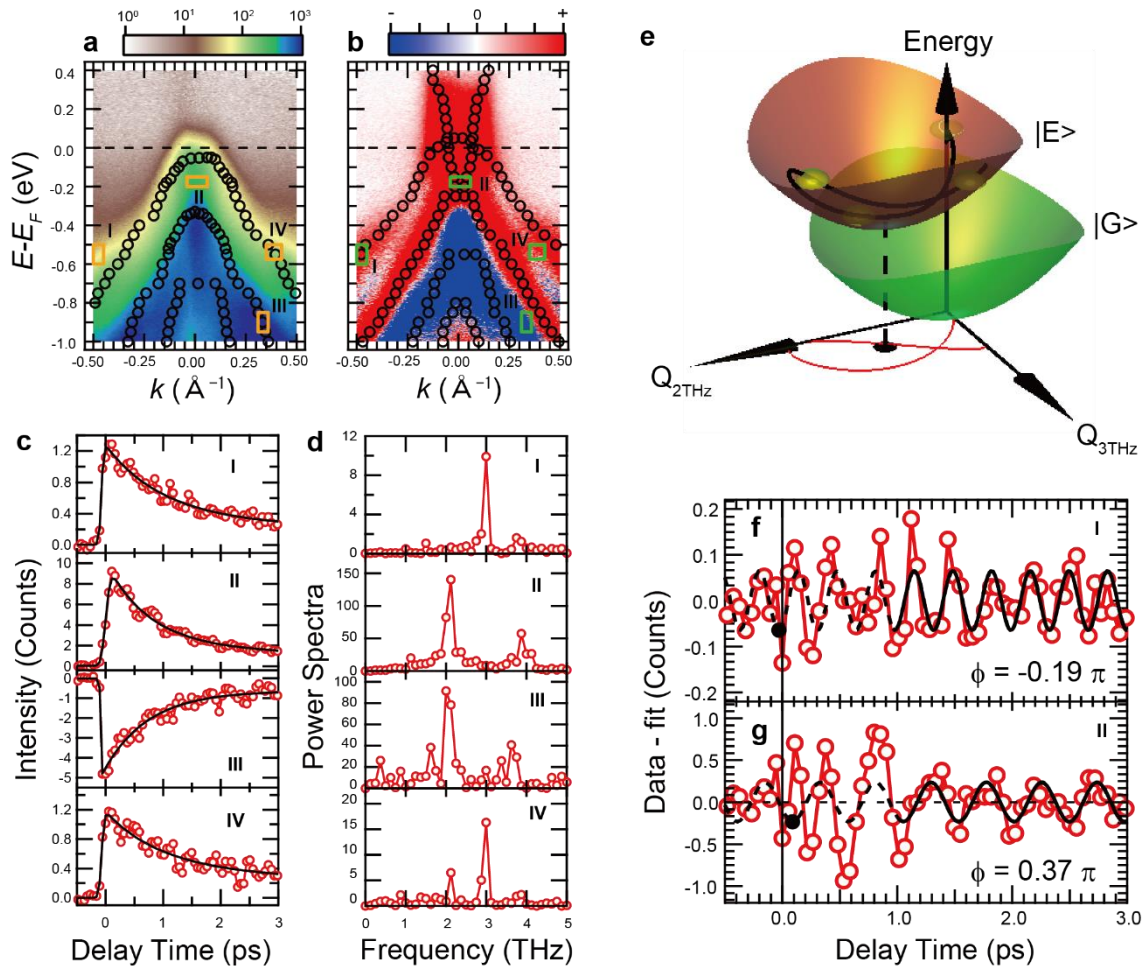


**Figure 2 | Time-to-frequency domain for intensities of TARPES spectra. a,b,** TARPES spectra before and after pump excitation. The peak positions in the TARPES spectra are indicated as circles. **c,** Time-dependent TARPES intensities at different energy and momentum regions. I–VI corresponds to the regions indicated in **a** and **b**. Data are shown as red circles whereas the fitting results by double-exponential decay functions convoluted with a Gaussian function are shown as black solid lines. **d,** Amplitude of Fourier transforms of the oscillation components in **c(I)–c(IV)** obtained by subtracting the fitting curve from the data. **e,** Schematic illustration of the free energy curves for the ground and photo-excited states as a function of lattice coordinates corresponding to the directions

of the 2-THz and 3-THz phonon modes. **f,g**, Oscillation components for I and II corresponding to the data subtracted by the fits. The fitting curve using a single cosine function are shown as dotted and solid black curves. We use data for the fits shown by solid black curves. The obtained phases are indicated in each panel.

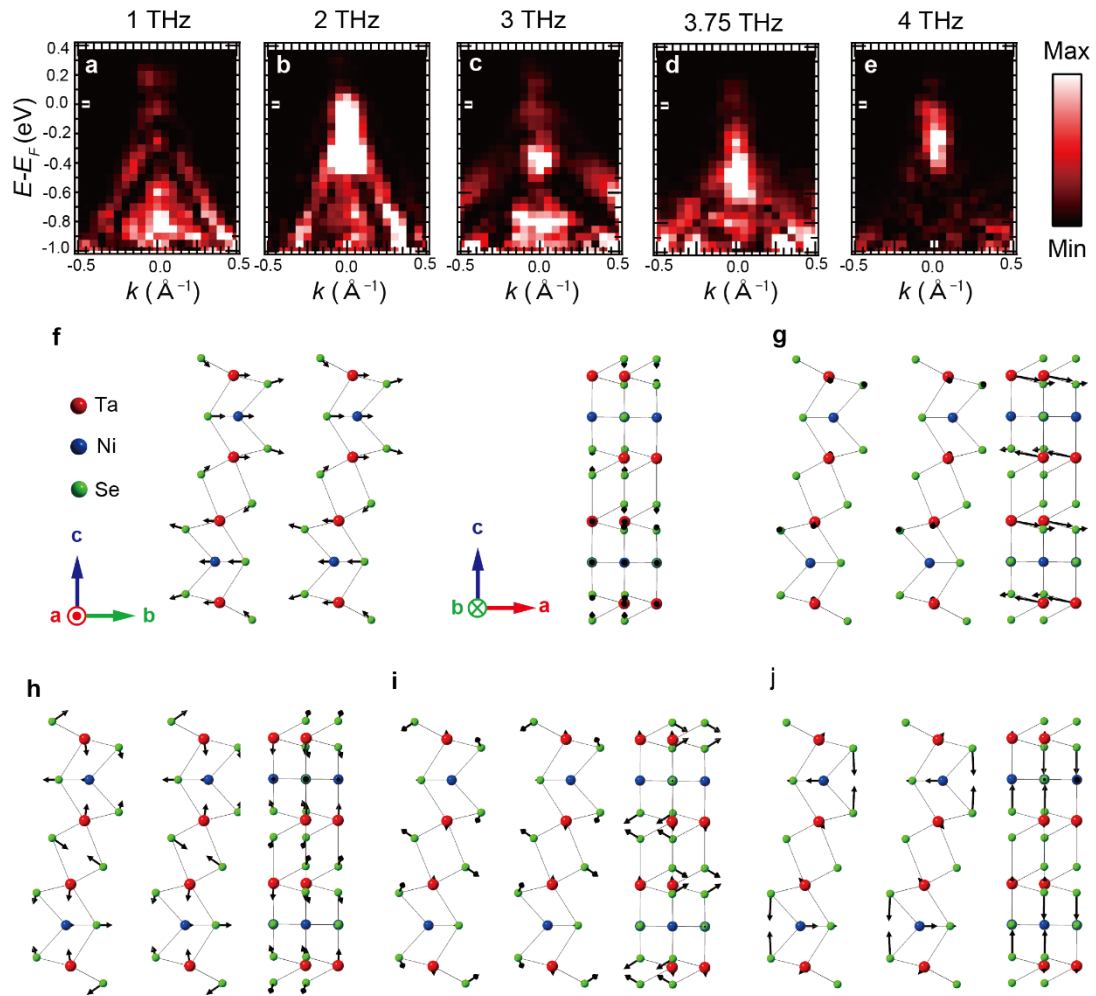


**Figure 3 | FDARPES spectra and corresponding phonon modes.** **a–e**, Frequency-domain angle-resolved photoemission spectroscopy (FDARPES) spectra shown as frequency-dependent intensities of the oscillation components as a function of energy and momentum. **f–j**, Calculated phonon modes corresponding to **a–e**.

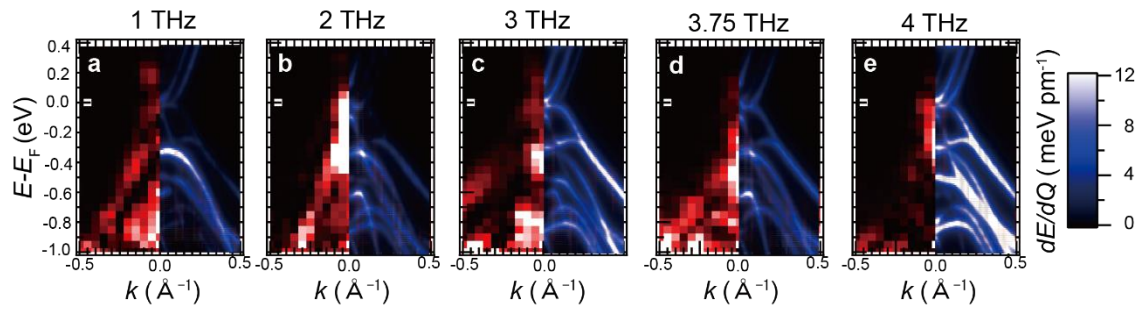


**Figure 4 | Calculation of FDARPES spectra. a–e,** FDARPES spectra (left panels) and calculated  $dE/dQ$ , (right panels) for each phonon mode.

## Supplementary information

Ref.

<https://www.nature.com/nature/for-authors/supp-info>

### **Physical description and simulation scheme**

Most coherent phonons excited by displacive excitation of coherent phonon (DECP) mechanisms [1] show a similar phonon frequency to ground state frequency evaluated with Raman scattering measurements [2-5]. The frequency-domain ARPES (FDARPES) spectra shown in Fig. 3a-3e are attributed to the Fourier transform of ARPES modulation owing to the coherent phonon excited by the pump pulse. To identify the phonon modes, we extracted electronic structure modulation due to phonon modes from theoretical simulations. We employed an *ab-initio* theoretical framework based on density-functional theory (DFT) [6, 7]. We evaluated the phonon modes and take all-symmetric modes, Ag irreducible representation, from the framework. By distorting the atomic position from equilibrium structure along with each phonon mode, we extracted the band-energy shifts with respect to the lattice modulation  $dE/dQ$ . This  $dE/dQ$  is the theoretical counterpart of the FDARPES experiment shown in Fig. 4.

### **Details of theoretical simulation**

Our theoretical simulation relied on the Perdew–Burke–Ernzerhof (PBE) functional [8] within density-functional theory (DFT). Whole calculations were performed by the

ABINIT code [9]. We used the fhi98PP pseudopotential [10] for abinit [11] with plane-wave basis set whose energy cut-off was chosen as 50 Hartree, 1361 eV.

To enforce the proper crystal spatial symmetry, C2/c (No. 15), we used the Bravais lattice which is twice of the primitive cell. We use the supercell for the atomic position optimization with the self-consistent field (SCF) and the phonon mode calculations with  $24 \times 6 \times 6$  Brillouin zone sampling. To obtain the band dispersion, we used the primitive cell with  $24 \times 24 \times 12$  Brillouin zone sampling for the SCF calculations.

Atomic position optimization

First, we performed atomic position optimization based on PBE-DFT with the same cell shape as an experimental value,  $a = 3.496 \text{ \AA}$ ,  $b = 12.829 \text{ \AA}$ ,  $c = 15.641 \text{ \AA}$ ,  $\alpha = \gamma = 90^\circ$ ,  $\beta = 90.53^\circ$  [12]. The tolerance of the optimization was  $5.0 \times 10^{-5}$  a.u. = 0.0257 eV nm<sup>-1</sup>. The DFT-optimal atomic and experimental positions are shown in Table 1 and Table 2. The input file for SCF within ABINIT is attached as supplemental material (input\_SCF.in).

**Table 1** Atomic positions of the optimal crystal structure from DFT

	x	y	z
Ta	-0.004440	0.220835	0.109287
Ni	0.0	0.701355	1/4
Se(1)	0.5046	0.077651	0.138568
Se(2)	-0.003119	0.142849	0.950279
Se(3)	0.0	0.32910	1/4

**Table 2** Atomic positions of the experimental crystal structure

	x	y	z
Ta	-0.007930	0.221349	0.110442
Ni	0.0	0.701130	1/4
Se(1)	0.5053	0.080385	0.137979
Se(2)	-0.005130	0.145648	0.950866
Se(3)	0.0	0.32714	1/4

Phonon mode calculation and its assignment

Second, we obtained phonon modes based on density-functional perturbation theory

(DFPT). [13] The normal mode  $U_{a,\alpha}^q$  for atom  $a$  was obtained as an eigenfunction of the dynamical matrix through DFPT as

$$\sum_{b\beta} \mathcal{D}_{a\alpha;b\beta} U_{b,\beta}^q = \omega^2(q) U_{a,\alpha}^q, \quad \alpha, \beta = x, y, z, \quad \sum_{\alpha} |U_{a,\alpha}^q|^2 = 1, \quad (1)$$

where  $q$  is an index for the eigenmode. The input file for DFPT within ABINIT is attached as supplemental material (input\_DFPT.in). The actual atomic displacement

was obtained by  $\delta R_{a,\alpha}^q = U_{a,\alpha}^q / \sqrt{M_a}$ , using mass  $M_a$  of an atom  $a$ . Because the

Bravais lattice is a double size supercell, the phonon modes obtained by DFPT contain

$\Gamma$ -point phonons and finite wavenumber phonons. Because the equivalent atomic

displacements of  $\Gamma$ -point modes is in-phase, the relative motions of the equivalent

atoms are the reference to extract the relevant phonon modes. We rejected modes that

showed counter displacements between two-equivalent atoms.

We identified an irreducible representation for each mode by performing symmetry operations for the atomic displacement and evaluating characters by symmetry operation for the general points of the Bravais lattice,

$$R_1 \begin{pmatrix} x_1 \\ x_2 \\ x_3 \end{pmatrix} = \begin{pmatrix} x_1 \\ x_2 \\ x_3 \end{pmatrix}, R_2 \begin{pmatrix} x_1 \\ x_2 \\ x_3 \end{pmatrix} = \begin{pmatrix} -x_1 \\ x_2 \\ -x_3 + 1/2 \end{pmatrix}, R_3 \begin{pmatrix} x_1 \\ x_2 \\ x_3 \end{pmatrix} = \begin{pmatrix} -x_1 \\ -x_2 \\ -x_3 \end{pmatrix}, R_4 \begin{pmatrix} x_1 \\ x_2 \\ x_3 \end{pmatrix} = \begin{pmatrix} x_1 \\ -x_2 \\ x_3 + 1/2 \end{pmatrix}, \quad (2)$$

and character table, Table 3.

**Table 3** Characters table of the C2/c space group

C2/c	R1	R2	R3	R4
Ag	1	1	1	1
Au	1	1	-1	-1
Bg	1	-1	1	-1
Bu	1	-1	-1	1

Numerically evaluated characters for the displacement were evaluated as

$$C_i^q = \sum_a \left[ (\delta r_{b,1}^q, \delta r_{b,2}^q, \delta r_{b,3}^q) \tilde{R}_i \begin{pmatrix} \delta r_{a,1}^q \\ \delta r_{a,2}^q \\ \delta r_{a,3}^q \end{pmatrix} \right] / \sum_a [(\delta r_{a,1}^q)^2 + (\delta r_{a,2}^q)^2 + (\delta r_{a,3}^q)^2], \quad (3)$$

where  $\delta r_a^q$  is the coordinate for the lattice vectors rather than Cartesian coordinate, atom  $b$  is that transformed by  $R_i$  from atom  $a$ , and  $\tilde{R}_i$  is a translation-free symmetry operation as

$$\tilde{R}_1 \begin{pmatrix} x_1 \\ x_2 \\ x_3 \end{pmatrix} = \begin{pmatrix} x_1 \\ x_2 \\ x_3 \end{pmatrix}, \tilde{R}_2 \begin{pmatrix} x_1 \\ x_2 \\ x_3 \end{pmatrix} = \begin{pmatrix} -x_1 \\ x_2 \\ -x_3 \end{pmatrix}, \tilde{R}_3 \begin{pmatrix} x_1 \\ x_2 \\ x_3 \end{pmatrix} = \begin{pmatrix} -x_1 \\ -x_2 \\ -x_3 \end{pmatrix}, \tilde{R}_4 \begin{pmatrix} x_1 \\ x_2 \\ x_3 \end{pmatrix} = \begin{pmatrix} x_1 \\ -x_2 \\ x_3 \end{pmatrix}, \quad (4)$$

because the displacement itself is a translation-free object. Errors of the numerical character were smaller than  $1.0 \times 10^{-5}$  compared with the expected unity.

We focused on the Ag mode because the DECP mechanism informs us that the all-symmetric Ag mode is excited. The frequencies are shown in Table 4. Actual modes are attached as supplemental material (PBE\_phonon.csv).

**Table 4** Frequencies of Ag mode, quasicharacters and assigned experimental modes

Frequency [THz]	Quasicharacter for orthorhombic phase	Assigned to experimental mode	C2	C4	C6	C8
0.99	Ag	1.08 THz	0.998	0.998	0.998	0.998
1.96	B2g	2.14 THz	-1.000	-1.000	-1.000	-1.000
2.42	B2g	3.71 THz	-0.979	-0.979	-0.979	-0.979
2.88	Ag	3.04 THz	-0.709	-0.709	-0.709	-0.709
3.57	Ag	4.07 THz	0.700	0.700	0.700	0.700
4.46	B2g		-0.998	-0.998	-0.998	-0.998
5.16	Ag		0.906	0.906	0.906	0.906
5.68	Ag		0.830	0.830	0.830	0.830
6.28	Ag		0.780	0.780	0.780	0.780
6.76	Ag		0.845	0.845	0.845	0.845
8.55	Ag		0.995	0.995	0.995	0.995

We assigned theoretical modes to an experimental frequency by the approximated symmetry of the oscillation. In Table 5, quasicharacters for the orthorhombic phase are shown as well. By increasing the temperature, the Ta<sub>2</sub>NiSe<sub>5</sub> crystal adopted an orthorhombic crystal structure, Cmcm (No. 63), whose operation and character table are given in Eq. (5) and Table 5, respectively. We numerically evaluated the characters based on the Cmcm symmetry and used its value to assign the phonon modes to whether Ag or B2g modes. This analysis was not rigorously well defined and is an approximated treatment. We called the numerically evaluated character for the higher symmetry space group as the quasicharacter here.

$$\begin{aligned}
C_1 \begin{pmatrix} x_1 \\ x_2 \\ x_3 \end{pmatrix} &= \begin{pmatrix} x_1 \\ x_2 \\ x_3 \end{pmatrix}, C_2 \begin{pmatrix} x_1 \\ x_2 \\ x_3 \end{pmatrix} = \begin{pmatrix} -x_1 \\ -x_2 \\ x_3 + 1/2 \end{pmatrix}, C_3 \begin{pmatrix} x_1 \\ x_2 \\ x_3 \end{pmatrix} = \begin{pmatrix} -x_1 \\ x_2 \\ -x_3 + 1/2 \end{pmatrix}, C_4 \begin{pmatrix} x_1 \\ x_2 \\ x_3 \end{pmatrix} = \begin{pmatrix} x_1 \\ -x_2 \\ -x_3 \end{pmatrix}, \\
C_5 \begin{pmatrix} x_1 \\ x_2 \\ x_3 \end{pmatrix} &= \begin{pmatrix} -x_1 \\ -x_2 \\ -x_3 \end{pmatrix}, C_6 \begin{pmatrix} x_1 \\ x_2 \\ x_3 \end{pmatrix} = \begin{pmatrix} x_1 \\ x_2 \\ -x_3 + 1/2 \end{pmatrix}, C_7 \begin{pmatrix} x_1 \\ x_2 \\ x_3 \end{pmatrix} = \begin{pmatrix} x_1 \\ -x_2 \\ x_3 + 1/2 \end{pmatrix}, C_8 \begin{pmatrix} x_1 \\ x_2 \\ x_3 \end{pmatrix} = \begin{pmatrix} -x_1 \\ x_2 \\ x_3 \end{pmatrix}, (5)
\end{aligned}$$

**Table 5** Characters table of the Cmcm space group

	C1	C2	C3	C4	C5	C6	C7	C8
Ag	1	1	1	1	1	1	1	1
Au	1	1	1	1	-1	-1	-1	-1
B1g	1	1	-1	-1	1	1	-1	-1
B1u	1	1	-1	-1	-1	-1	1	1
B3g	1	-1	-1	-1	1	-1	-1	1
B3u	1	-1	-1	1	-1	1	1	-1
B2g	1	-1	1	-1	1	-1	1	-1
B2u	1	-1	1	-1	-1	1	-1	1

To obtain the quasicharacter, we introduced an approximated identification of the atomic position related to Eq. (5). We allowed error value  $\epsilon = 0.1$  Bohr = 0.00592 nm for the identification as

$$\sqrt{\left[ \sum_{p\alpha} A_{\alpha,p} (C_i r_{a,\alpha} - r_{b,\alpha}) \right]^2} < \epsilon, \quad (6)$$

where  $r_{a,\alpha}$  is the reduced coordinate of atom  $a$  and  $A$  is a matrix to convert the reduced coordinate to a Cartesian coordinate. The error value was chosen such that a one-to-one correspondence of atoms was realized for the whole operation given by Eq. (5). Although the fourth Ag mode, 2.88 THz, had an almost B2g-like character, we assigned it as an Ag mode. In the orthorhombic phase, the number of B2g mode is three. We assign three modes, 1.96 THz, 2.42 THz, and 4.46 THz, that had the closest quasicharacter value compared to minus unity as the B2g mode and do not 2.88 THz mode.

Band calculation for distorted crystal

Finally, we performed band structure calculations of the distorted atomic positions with the primitive cell, identified as  $a' = b' = 6.648$  Å,  $c' = 15.641$  Å,  $\alpha' = \beta' = 90.14^\circ$ ,  $\gamma' = 149.51^\circ$ . In the DFT-optimal structure case, band structures were obtained for equilibrium (Fig. S1a) and slightly displaced atomic positions along with the phonon modes (Fig. S1b–d). The amounts of displacement were determined based on the root squared mean as,

$$R_{a,\alpha}(q) = R_{a,\alpha}^{\text{eq}} + \Delta_{a,\alpha}(q), \quad \Delta_{a,\alpha}(q) = c_q \frac{U_{a,\alpha}}{\sqrt{M_a}}, \quad \sqrt{\frac{1}{N_{\text{atom}}} \sum_{a,\alpha} [\Delta_{a,\alpha}(q)]^2} = 0.1 \text{ pm}. \quad (7)$$

where  $N_{\text{atom}}$  is the number of atoms in the unit cell. One should note that the overall displacement direction of the normal mode randomly appears by numerical diagonalization, namely a set of inverse displacements is also the solution of the dynamical matrix. To obtain consistent band-energy for each atomic position, the band dispersion is always measured by the Fermi levels of each calculations. This implicitly means that the electron suddenly follows atomic motion, namely adiabatic approximation. By taking the absolute value of the band-energy shifts for the displaced position from the equilibrium positions,  $dE/dQ$ , the theoretical counter part of the FDARPES data is obtained. The results with the opposite displacements showed quite similar absolute value of  $dE/dQ$ , which meant this displacement amount was in the almost linear regime for the band-structure change. We converted the band dispersions along the  $\Gamma$ -X line into  $k$ -resolved density of states ( $k$ -DoS) by convoluting with a

$$\text{Lorentzian, } D(\omega, k) = \sum_b \frac{\delta_\omega}{\pi} \frac{1}{(\omega - \epsilon_{bk})^2 + \delta_\omega^2} \frac{\delta_k}{\pi} \frac{1}{(k - k_{b\omega})^2 + \delta_k^2}, \delta_\omega = 0.001 \text{ eV, } \delta_k =$$

$0.001 \text{ \AA}^{-1}$ . The convolution results are shown in Fig. S1e–h.

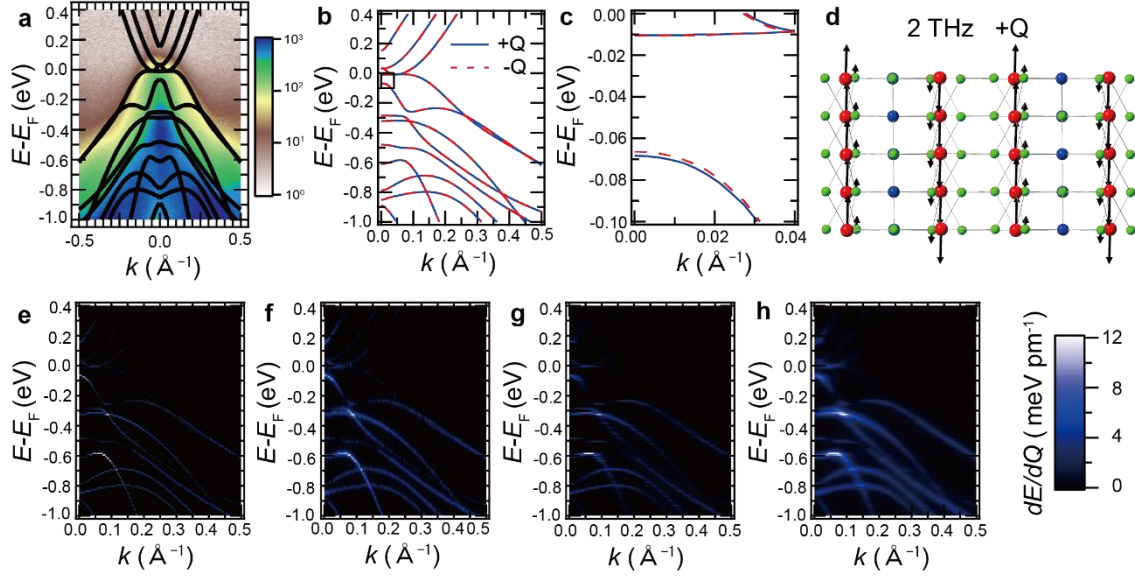


**Figure S1** Figure with PW-DFT. **a.** Band structure at equilibrium. The calculation results are shown as black solid lines, while the ARPES image is taken using a He-discharge lamp. **b,c.** Calculated band structure for slightly displaced atomic positions corresponding to the 2-THz phonon mode. **d.** 2-THzPhonon mode. **e.** Energy shifts with respect to the lattice modulation  $dE/dQ$ . **f-h.**  $k$ -DoS for  $dE/dQ$  by convoluting with a Lorentzian function. Convolutions are performed along  $E$ - and  $k$ -directions for **f** and **g**, respectively, whereas convolutions along both  $E$  and  $k$  directions are performed in **h**.

Follow-up

To check robustness of our conclusion with this specific framework based on PBE-DFT, we performed calculations in different conditions, 1) Perdew-Wang (PW) functional [14] was used rather than PBE, 2) PBE-DFT framework but with experimental atomic positions, and 3) PW-DFT framework with experimental atomic positions. We use LDA pseudopotential [15] for the PW-DFT calculations, which is shown in Fig. S2. The atomic position optimized with the PW functional is shown in Table 6. To obtain the identification of approximately equivalent atoms for the orthorhombic phase,  $\epsilon = 0.2$  Bohr was employed in Eq. (6) for the experimental crystal structure.

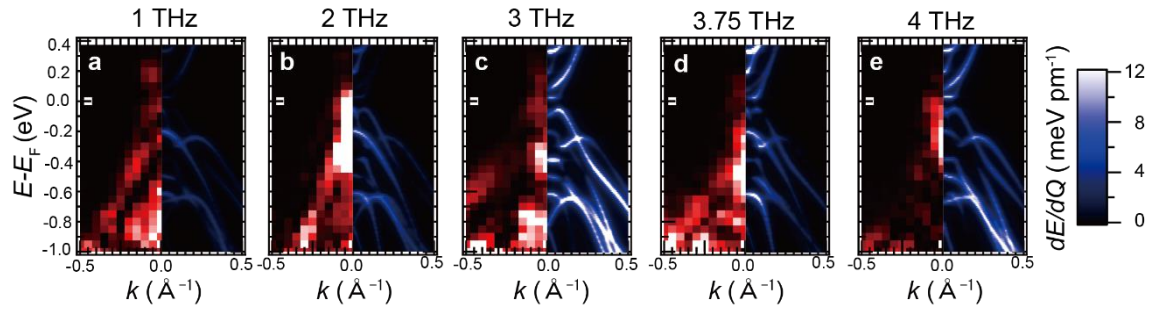


**Figure S2** Calculation of FDARPES spectra using PW-DFT framework and LDA pseudopotential. **a–e**, FDARPES spectra (left panels) and calculated  $dE/dQ$  (right panels) for each phonon mode.

**Table 6** Atomic position of DFT with the PW functional

	x	y	z
Ta	-0.007407	0.223358	0.112221
Ni	0.0	0.7049391	1/4
Se(1)	0.5047	0.077647	0.138656
Se(2)	-0.004972	0.149029	0.952662
Se(3)	0.0	0.32730	1/4

**Table 7** Phonon frequencies and quasicharacter

Frequenc y [THz] (PW DFT)	Quasicharacte r (PW DFT)	Frequenc y [THz] (PBE Exp.)	Quasicharacte r (PBE Exp.)	Frequenc y [THz] (PW Exp.)	Quasicharacte r (PW Exp.)
0.97	Ag	0.96	Ag	1.05	Ag
1.91	B2g	2.03	B2g	1.78	B2g
2.88	Ag	2.83	Ag	2.61	B2g
3.14	B2g	3.53	B2g	2.85	Ag
3.72	Ag	3.59	Ag	3.65	Ag
4.57	B2g	4.64	B2g	4.29	B2g
5.16	Ag	5.32	Ag	5.01	Ag
5.67	Ag	5.89	Ag	5.38	Ag
6.21	Ag	6.45	Ag	6.01	Ag
6.92	Ag	7.04	Ag	6.56	Ag
8.80	Ag	8.86	Ag	8.38	Ag

The same plot as Fig. 4 in the main manuscript but with the PW functional is shown in Figure S2. The band dispersion change arising from atomic displacement was mainly characterized by the character of the modes, with the B2g modes leading to the strong influence of the  $\Gamma$  point.

Here, we comment on a trade-off between the computational cost and convergence accuracy of the results of this simulation. The most computationally demanding part of this procedure was the DFPT part because many and large linear systems must be

solved. When 384 cores of the system-B (Sekirei), supercomputer at the Institute of Solid State Physics, the University of Tokyo, were used within the flat-MPI parallelization, the DFPT calculation took 65.13 hours. Roughly speaking, the DPFT cost with the GGA-functional obeys a linear scaling for the number of k-points. An estimation for  $36 \times 9 \times 9$  Brillouin zone sampling is 21 hours, with 3,600 cores. This calculation is possible in principle but hardly achievable with the supercomputer system.

**Table 8** Atomic positions of optimal crystal structure from PBE-DFT with  $36 \times 9 \times 9$  Brillouin zone sampling

	x	y	z
Ta	-0.004442	0.220801	0.109289
Ni	0.0	0.7013654	1/4
Se(1)	0.5046	0.077653	0.138552
Se(2)	-0.003147	0.142847	0.950286
Se(3)	0.0	0.32910	1/4

To evaluate the convergence accuracy with respect to the density of Brillouin zone sampling, we estimated the error through the residual error of the force and equilibrium atomic position for denser Brillouin zone sampling,  $NK=36 \times 9 \times 9$ . The residual force, evaluated with the optimal atomic position of sparser Brillouin zone sampling, was maximally  $1.3 \times 10^{-4} = 0.068 \text{ eV nm}^{-1}$ , which was fairly close to our criteria to identify the atomic equilibrium position. The optimized atomic positions with denser sampling are shown in Table 8. By converting these to a Cartesian coordinate, maximal error is

$6.8 \times 10^{-6}$  [a.u.] = 0.36 fm. These errors were small compared with the following case

for the energy cut off.

We also checked the energy convergence error by using energy cut off 60 a.u. = 1633

eV with the same Brillouin zone sampling,  $NK = 24 \times 6 \times 6$ . The residual force,

evaluated with  $ecut = 50$  a.u., is maximally  $2.2 \times 10^{-4}$  a.u. = 0.11 eV nm<sup>-1</sup>. The

optimized atomic positions are shown in Table 9. The maximal error of the atomic

position in the Cartesian coordinate was  $1.3 \times 10^{-5}$  a.u. = 0.69 fm. Performing DFPT

calculation for the energy cut off 60 a.u., we obtained the phonon frequencies and

quasicharacter shown in Table 10. The error for the frequency of the phonon modes was

maximally 0.02 THz. Thus, the error in the Brillouin zone sampling is expected to be

smaller than this error.

**Table 9** Atomic positions of optimal crystal structure from PBE-DFT with energy cut off 60 a.u.

	x	y	z
Ta	-0.004440	0.220819	0.109280
Ni	0.0	0.7014205	1/4
Se(1)	0.5046	0.077647	0.138557
Se(2)	-0.003124	0.142859	0.950281
Se(3)	0.0	0.32910	1/4

**Table 10** Phonon frequencies of optimal crystal structure from PBE-DFT energy cut off 60 a.u.

Frequency [THz]	Quasicharacter for orthorhombic phase	C2	C4	C6	C8
0.97	Ag	0.998	0.998	0.998	0.998
1.96	B2g	-1.000	-1.000	-1.000	-1.000
2.42	B2g	-0.979	-0.979	-0.979	-0.979
2.87	Ag	-0.713	-0.713	-0.713	-0.713
3.56	Ag	0.684	0.684	0.684	0.684
4.46	B2g	-0.998	-0.998	-0.998	-0.998
5.16	Ag	0.900	0.900	0.900	0.900
5.67	Ag	0.830	0.830	0.830	0.830
6.28	Ag	0.780	0.780	0.780	0.780
6.76	Ag	0.844	0.844	0.844	0.844
8.53	Ag	0.995	0.995	0.995	0.995

## References

- [1] Zeiger, H. J., Vidal, J., Cheng, T. K., Ippen, E. P., Dresselhaus, G., & Dresselhaus, M. S. *Phys. Rev. B* **45**, 768 (1992).
- [2] Misochko, O. V. & Lebedev, M. V. *J. Exp. Theor. Phys.* **126** 64 (2018).
- [3] Garrett, G. A., Albrecht, T. F., Whitaker, J. F., & Merlin. R. *Phys. Rev. Lett.* **77**, 3661 (1996).
- [4] Ishioka, K., Kitajima, M., & Misochko, O. V. *J. Appl. Phys.* **103**, 123505 (2008).
- [5] Werdehausen, D., Takayama, T., Höppner, M., Albrecht, G., Rost, A. W., Lu, Y., Manske, D., Takagi, H. & Kaiser, S. *Sci. Adv.* **4**, eaap8652 (2018).
- [6] Hohenberg, P. & Kohn., W. *Phys. Rev.* **136**, B864 (1964).
- [7] Kohn, W. & Sham, L. J. *Phys. Rev.* **140**, A1133 (1965).
- [8] Perdew, J. P., Burke, K., & Ernzerhof, M. *Phys. Rev. Lett.* **77**, 3865 (1996).

- [9] Gonze, X. *et al.*, Comput. Phys. Commun. **205**, 106-131 (2016).
- [10] Fuchs, M. & Scheffler, M. Comput. Phys. Commun. **119**, 67 (1999).
- [11] [https://www.abinit.org/sites/default/files/PrevAtomicData/psp-links/gga\\_fhi.html](https://www.abinit.org/sites/default/files/PrevAtomicData/psp-links/gga_fhi.html)
- [12] Sunshine, S. A. & Ibers, J. A. Inorg. Chem. **24**, 3611 (1985).
- [13] de Gironcoli, B. S., Dal Corso, A. & Giannozzi, P. Rev. Mod. Phys. **73**, 515 (2001).
- [14] Perdew, J. P., & Wang, Y. Phys. Rev. B **45**, 13244 (1992).
- [15] [https://www.abinit.org/sites/default/files/PrevAtomicData/psp-links/lda\\_fhi.html](https://www.abinit.org/sites/default/files/PrevAtomicData/psp-links/lda_fhi.html)